Interpretable Quality Control of Sparsely Distributed Environmental Sensor Networks Using Graph Neural Networks

Elżbieta Lasota,[a] Timo Houben,[b,c] Julius Polz,[a] Lennart Schmidt,[b,c] Luca Glawion,[a] David Schäfer,[b,c] Jan Bumberger,[b,c,d] and Christian Chwala[a]

[a] *Institute of Meteorology and Climate Research Atmospheric Environmental Research, Karlsruhe Institute of Technology KIT, Kreuzeckbahnstraße 19, 82467 Garmisch-Partenkirchen, Germany,* [b] *Research Data Management - RDM, Helmholtz Centre for Environmental Research - UFZ, Permoserstraße 15, 04318 Leipzig, Germany,* [c] *Department of Monitoring and Exploration Technologies, Helmholtz Centre for Environmental Research - UFZ, Permoserstraße 15, 04318 Leipzig, Germany,* [d] *German Centre for Integrative Biodiversity Research (iDiv) Halle-Jena-Leipzig, Puschstraße 4, 04103 Leipzig, Germany*

Corresponding author: Elżbieta Lasota, elzbieta.lasota@kit.edu

ABSTRACT: Environmental sensor networks play a crucial role in monitoring key parameters essential for understanding Earth's systems. To ensure the reliability and accuracy of collected data, effective quality control (QC) measures are essential. Conventional QC methods struggle to handle the complexity of environmental data. Conversely, advanced techniques such as neural networks, are typically not designed to process data from sensor networks with irregular spatial distribution. In this study, we focus on anomaly detection in environmental sensor networks using graph neural networks, which can represent sensor network structures as graphs. We investigate its performance on two datasets with distinct dynamics and resolution: commercial microwave link (CML) signal levels used for rainfall estimation and SoilNet soil moisture measurements. To evaluate the benefits of incorporating neighboring sensor information for anomaly detection, we compare two models: Graph Convolution Network (GCN) and a graph-less baseline-long short-term memory (LSTM). Our robust evaluation through 5-fold cross-validation demonstrates the superiority of the GCN models. For CML, the mean area under curve values for the GCN was 0.941 compared to 0.885 for the baseline-LSTM, and for SoilNet, it was 0.858 for GCN and 0.816 for the baseline-LSTM. Visual inspection of CML time series revealed that the GCN proficiently classified anomalies and remained resilient against rain-induced events often misidentified by the baseline-LSTM. However, for SoilNet, the advantage of GCN was less pronounced likely due to a fragile labeling strategy. Through interpretable model analysis, we demonstrate how feature attributions vividly illustrate the significance of neighboring sensor data, particularly in distinguishing between anomalies and expected changes in signal level in the time series.

1. Introduction

Climate information is the key ingredient for successful climate change adaptation and the mitigation of impacts of extreme events. Accurate and dense climate observations are essential for risk management and the prediction of natural hazards. However, there is a large gap in the global availability of climate information, especially in developing countries (UNFCCC 2022; Lorenz and Kunstmann 2012). To close this gap, multiple options are available. First, the installation of cost- and maintenance-intensive dedicated sensors like in the ICOS or TERENO observatories (Bogena 2016; Rebmann et al. 2018). Second, the usage of existing infrastructure like commercial microwave links (CMLs) for precipitation estimation (Chwala and Kunstmann 2019). Third, low-cost sensors like personal weather stations (Graf et al. 2021).

a. Quality control of environmental sensor data

A common theme to all efforts to observe the Earth's environment outside of controlled laboratory settings is the need for extensive quality control (QC) of the data. Inevitably, environmental sensors are subject to numerous disruptive influences and, thus, exhibit erroneous data, manifesting as unacceptable deviations from the expected value or ground truth of the measured variable. Causes include instrument constraints such as battery voltage and malfunction, technical failures during data transmission, or environmental influences that interfere with the measurement principle (Gandin 1988). Common QC approaches are: 1) Manual data inspection by domain experts – a task that lacks reproducibility nor explainability and that is often too laborious for operational data processing of large data volumes (Jones et al. 2018). 2) Automated workflows set up via rule-based or parametric statistical tests such as defining rules for physically plausible value limits or outliers with respect to a given statistical distribution (Schmidt et al. 2023; Horsburgh et al. 2015). Still, finding the right parametrization and test suite involves time-consuming trial-and-error and requires significant expert knowledge, especially if taking cross-dependencies between sensors or variables into account (Sturtevant et al. 2021). 3) deep learning (DL) algorithms for anomaly detection which promise to provide robust automated QC routines. They possess the capability to process and learn from diverse and extensive datasets, enabling them to capture complex relationships that traditional rule-based methods may overlook. Despite varying requirements for accurately labeled training data depending on the complexity of the problem (Erhan et al. 2021; Wang et al. 2022), their ability to autonomously learn from data enhances their versatility and effectiveness in QC tasks. However, DL methods are often considered black boxes, meaning that the models' decisions are not self-explanatory and hard to interpret.

b. Deep learning for anomaly detection

In this study, we focus on the methodological development of improved DL approaches for QC of environmental sensor data. DL has been extensively applied in fields such as cybersecurity, medicine, food industry, or manufacturing (Zhang et al. 2021; Vandewinckele et al. 2020; Nayak et al. 2020; Cioffi et al. 2020). However, most studies benefited used ready-to-use benchmark datasets, enabling comparison of algorithm performance across different studies (Erhan et al. 2021). Currently, the few applications of anomaly detection on real-world environmental sensor networks primarily focus on detecting anomalies in uni- or multi-variate time series of single sensors using well-established methods such as auto-regressive integrated moving average, support vector machines, and long short-term memory (LSTM) models (Russo et al. 2021; Jones et al. 2022; Muharemi et al. 2019). There has been relatively little emphasis on addressing the challenges associated with DL-based QC of sensor networks considering neighboring sensor information. These challenges include sparsity in space due to irregular sensor network layouts and variations in data availability resulting from evolving network layouts and sensor malfunctions.

Considering not only single-sensor but also contextual anomalies it can be assumed that the signals from multiple sensors distributed across space and their interrelationships help in detecting erroneous behavior (Chalapathy and Chawla 2019). Thus, a neural network architecture capable of encoding the spatial proximity of sparse and variable inputs is essential to enhance DL-based anomaly detection. One approach that can suit these needs is using Graph Neural Networks (GNNs) which have a remarkable capability to handle irregular and unstructured data containing relational information, which can be naturally represented as graphs. Traditional neural networks are more tailored to process structured data such as images, individual sequences, or rasters (Egmont-Petersen et al. 2002; Zhang et al. 2022; Sutskever et al. 2014). Existing GNN applications cover diverse domains, including social network analysis, recommendation systems, and chemistry (Fan et al. 2019; Zhang et al. 2022; Coley et al. 2019). There are several well-performing GNN applications for anomaly detection in controlled experiments like benchmark datasets, synthetic pollution events in air quality data, or simulated attacks on waste-water test-bed systems (Guan et al. 2022; Lin et al. 2022; Deng and Hooi 2021). However, an application of GNNs for QC of sparse, real-world environmental sensor networks has not been studied.

c. The need for explainable AI

Crucial requirements for QC in an operational setting are interpretability and reproducibility of classification results. While reproducibility is achieved by establishing and sharing a deterministic algorithm, the interpretability of neural network outputs requires its own set of dedicated techniques summarized under the term explainable artificial intelligence (XAI). Generally, XAI for GNNs is an active field of research that majorly encompasses theoretical work (Agarwal et al. 2022). Gradient-based XAI methods analyze gradients with respect to neural network input-output pairs in order to attribute model predictions to input features. Several gradient-based methods for GNNs were proposed (Baldassarre and Azizpour 2019; Pope et al. 2019) but there are only few applications (Kosasih and Brintrup 2022; Rathee et al. 2022; Yin et al. 2023). An evaluation of XAI for interpretability of GNN-based QC of environmental time series sensor data is yet missing.

d. Study outline

To close the above-mentioned knowledge gaps, this study aims to answer the following two research questions:

1) Can GNNs improve automated QC of environmental sensor data by integrating spatial information from sensor networks that are distributed irregularly in space and provide varying amounts of observations for each timestep?

2) Can XAI reveal information about the influence of neighboring sensors to explain the decisions of the proposed Graph Convolution Network (GCN) model?

To achieve comprehensive answers to these questions we selected two different datasets, one with CML signal level observations from a large network scattered across Germany, and one with soil moisture observations placed in a local-scale environmental observatory. Both datasets represent environmental sensors and share challenges such as irregular distribution in space, sensitivity to environmental factors, and a high number of sensors resulting in a large volume of observed data.

Differences include variable dynamics, spatial coverage, spatial resolutions, and sampling rate. These differences define the context in which results from this specific study may be generalized.

2. Methods

a. Data

1) Commercial microwave links

CMLs provide line of sight radio connections in mobile phone networks (Chwala and Kunstmann 2019). Since the wavelength of the transmitted signal is in the order of magnitude of raindrop diameters, the signal is significantly attenuated by rainfall through scattering and absorption processes (Atlas and Ulbrich 1977). CMLs. This offers an opportunity to accurately estimate rainfall amounts since the rainfall-induced path-integrated attenuation is related to the path-averaged rainfall rate in a close-to-linear manner (Messer et al. 2006). Additionally, the global coverage of inhabited areas by CMLs is extensive with more than 90% of the human population living in regions with broadband telecommunication access (GSMA 2022). However, other causes like dew formation on the antenna, multi-path propagation, or mixed-phase precipitation lead to fluctuations of the signal level thus disturbing accurate measurements (van Leth et al. 2018).

The CML data used in this study is a subset of a larger dataset collected in cooperation with Ericsson Germany using a custom CML data acquisition system (Chwala et al. 2016). The full dataset covers 3904 CMLs across all of Germany. The length of CML paths ranges from 0.1 km to more than 30 km and the transmission frequencies range from 10 to 40 GHz. For each CML, received signal level (RSL) and transmitted signal level (TSL) are recorded at a temporal resolution of 1 min and power resolutions of 0.3 dB and 1.0 dB for RSL and TSL, respectively. The difference between TSL and RSL yields total signal loss (TL), which is available for two sublinks per CML due to a two-way data transmission.

The subset we use in this study is focused on 20 CMLs that have been manually checked and labeled by four independent experts for March, May, and July 2019 using a specifically designed tool for visualization and labeling (Polz et al. 2023). Each expert categorized anomalies into different classes (jump, dew, fluctuation, and unknown). Since this study focuses on anomaly detection as a binary classification problem, assigning a single flag required agreement from at least three experts regarding the specific anomaly type. For each of the 20 quality-checked CMLs,

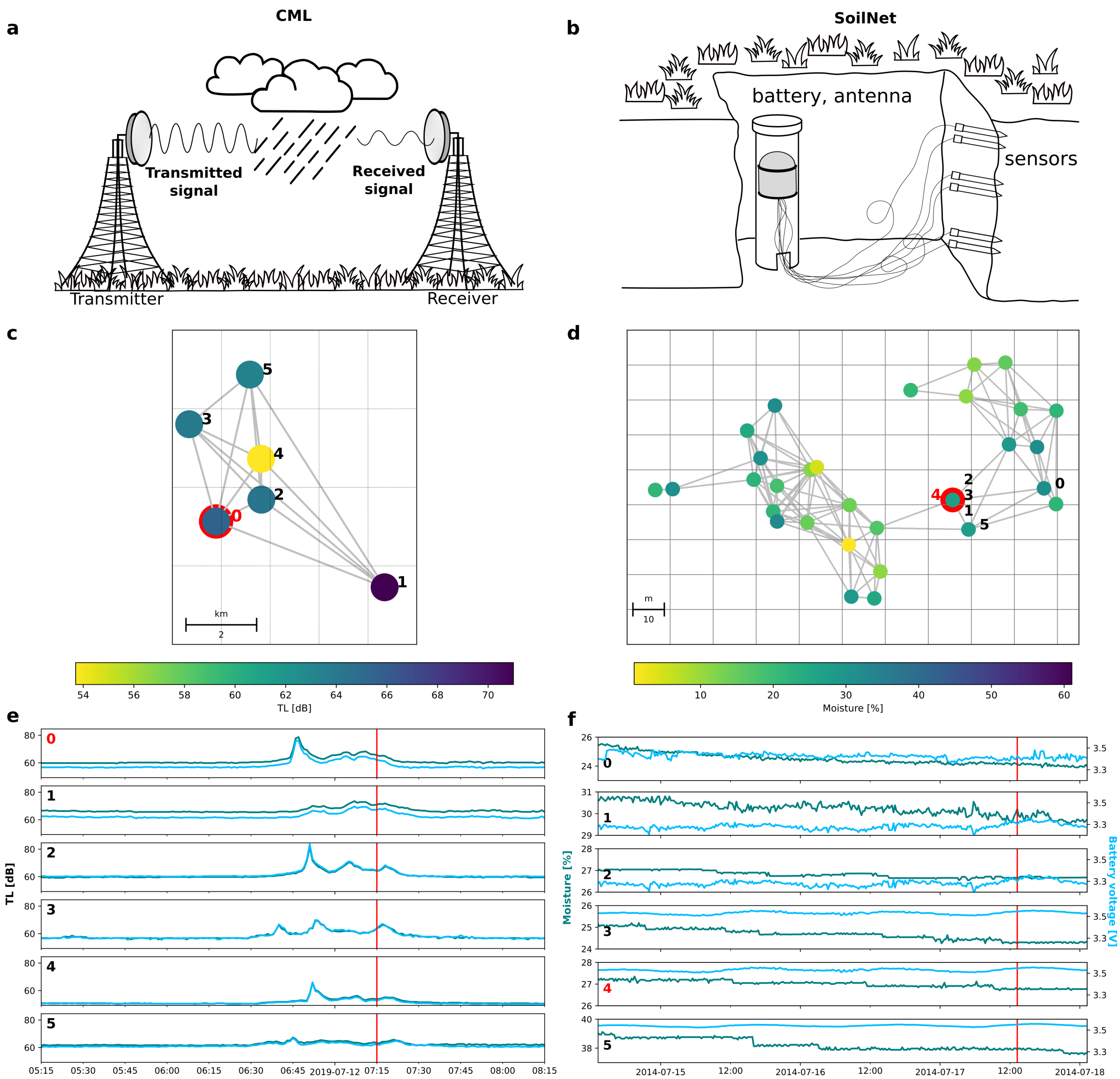

FIG. 1. Example of CML (left panels) and SoilNet (right panels) data used as input for the GCN models. Panels (a) and (b) illustrate the basic principles of CML and SoilNet techniques, respectively. Panel (c) illustrates the spatial connections between sensors at the classification time. Panel (d) depicts the SoilNet network configuration, considering its 3D structure in establishing links. Nodes' colors in the graphs represent TL and moisture values. Panel (e) displays the TL time series of labeled sensors (highlighted in red) and their neighbors. Similarly, panel (f) presents the time series of soil moisture and battery voltage for the labeled sensor (red) and its neighbors. In both panels, red vertical lines mark classification times.

the data from a selected set of neighboring CMLs is also included as illustrated by the example in Fig. 1. The neighbor selection procedure is described in Section 3).

2) SoilNet

SoilNet sensor networks are used for battery-operated wireless soil moisture and soil temperature measurements, in this case using SPADE soil moisture probes (Bogena et al. 2010).

The SoilNet data used in this study is a subset of continuous measurements at the Hohes Holz observatory, which is part of the TERENO Harz/Central German Lowland Observatory (Wollschläger et al. 2017). The site Hohes Holz is a 1 ha-patch of mixed beech forest where meteorological, hydrological, and ecological variables are observed at high spatial and temporal resolutions (Rebmann et al. 2017). The dataset comprises measurements of soil moisture (vol %) measured via the capacitance method, soil temperature measured by an integrated digital thermometer (°C), and battery voltage of the data acquisition platine for 2014. The variables were measured at a 15 minute temporal resolution in a network consisting of 180 sensors distributed over 35 spatial sampling locations at irregular spacing. At each sampling location, six sensors were vertically aligned below the soil surface, positioned at approximately 0.1 m intervals up to a depth of 0.6 m.

Generally, errors in soil moisture measurements stem from the diverse nature of soil properties and environmental factors (Mittelbach et al. 2012). Temperature fluctuations, improper sensor installation, or calibration errors may introduce inaccuracies. Additionally, the evolving presence of roots, stones, and preferential flow pathways in the soil can lead to spatial variability in moisture content (Mittelbach et al. 2012; SU et al. 2014). For the site at hand, battery voltage drops, transmission errors, and sensor deterioration over time were observed as additional sources of measurement errors.

The dataset was quality-checked using a semi-automated routine consisting of three automated tests and subsequent manual checking. The first automated test, the *Range* test, flagged data points that lie outside a physically plausible value range (for soil moisture between 5 % to 60 % and for soil temperature from -25 to 50 °C). Next, a custom *Spike* test flagged physically implausible jumps and outliers in soil moisture and soil temperature. Lastly, the *BattV* test flagged both soil moisture and soil temperature if the battery voltage dropped below 3 V. As these automated routines were not sufficient, all data was manually checked and, if necessary, flagged by domain experts. While the flagging was done by several experts during the measurement campaign, only one expert flagged one specific period. In this study, we focus on the automated detection of manually labeled anomaly flags and non-anomalous data.

3) Data preprocessing

Before the actual AI-model development, we prepared both datasets to optimize their quality and suitability for the model training to achieve the best performance. First, we selected relevant features for both datasets. For CML we used TL from both channels while we included moisture, battery voltage, and temperature for SoilNet. Subsequent preprocessing steps involved graph sample preparation with adjacency matrix establishment, missing data imputation, data normalization, and splitting the time series into fixed-length samples. All parameters for preprocessing were optimized experimentally.

In the CML dataset, only 20 out of almost 4000 sensors were flagged, while their neighbors were not quality-checked. In contrast, all sensors included in the SoilNet dataset were labeled. This difference in label availability required distinct approaches to preparing the samples for both datasets. Due to the limited availability of flagged CML sensors, to form a graph sample for GCN models, all sensors in a 20 km radius around a flagged CML were selected as graph nodes, and nodes with a maximum distance of 10 km were connected by edges. For SoilNet, all available sensors at the given time step were used as nodes and, due to 3D structure (longitude, latitude, and depth), the sensors were connected forming edges if they were within a 30 m distance and shared the same depth, or if they were located at the same position and within a vertical distance of up to 0.1 m.

Following the graphs definition, we proceeded to generate time series samples for training and testing. To increase the number of available samples, we applied linear gap interpolation in time, filling up to 5 missing data points, up to 5 minutes for CML data, and up to 60 minutes for SoilNet data.

Afterward, we normalized the data. For CML, 'rolling median removal' was employed, which has proven to be efficient for CML application (Polz et al. 2020), where the median value from the original time series for the five days prior to the classification time was subtracted. For SoilNet, we applied a min-max scaler based on variable-specific criteria: moisture ranged from a minimum of 0 to a maximum of 60, battery voltage from a minimum of 2800 to a maximum of 3600, and temperature between a minimum of -20 and a maximum of 40.

Then, the dataset was partitioned into time series samples of varying lengths. The time series length comprised 120 minutes and 72 hours before the flagged time step and 60 minutes and 12 hours after, for CML and SoilNet, respectively.

Samples containing any missing values after interpolation were excluded which can lead to gaps in a classification time series larger than the missing period (see ”no data” in Fig. 5). In the case of SoilNet, we also omitted samples that were flagged by automated QC tests, resulting in the final dataset encompassing solely manual flags and non-anomalous data. Eventually, the sample selection and preparation procedure resulted in 2 558 577 samples for CML and 18 639 samples, comprising a total of 2 588 730 nodes used for model development, for SoilNet. Illustrations of exemplary CML and SoilNet graphs and time series are depicted in Fig. 1.

b. GNN for anomaly detection

In this study, we leverage the power of GNN, specifically focusing on the core operation of graph convolution (GC), to tackle anomaly detection in environmental sensor networks. To comprehensively evaluate the efficacy of our GC-based anomaly detection framework and assess the advantages of incorporating neighboring sensor information, we introduce and compare two distinct models: the GCN model that uses neighboring sensor information and a corresponding baseline-LSTMs model that does not.

1) Graph neural network

The fundamental components of every graph are its nodes (V) and edges (E), where nodes ($v_i \in V$) represent entities and edges ($e_{ij} \in E$) draw relationships between nodes v_i and v_j. The arrangement of these elements is captured by the square adjacency matrix A, where A_{ij} is an entry indicating the presence (or absence) of an edge between nodes i and j. The basic concept underlying GNNs involves the simultaneous processing of information from node features and their interconnected neighbors, as defined by the edges, enabling the propagation of information throughout the graph. This fundamental operation is termed GC and comprises several sequential steps. Initially, node embedding is conducted by associating each node with a feature vector $h_v^{(0)}$.

Subsequently, exploiting the adjacency matrix A, information is aggregated from all neighboring nodes to update the nodes' representations. A typical representation of the update rule in graph convolution involves a transformation with learnable parameters, and optionally, an activation function, which may be expressed by the rule: (Kipf and Welling 2016; Chen et al. 2020; You et al. 2020):

$$H^{(l+1)} = \sigma\left(\tilde{D}^{-1/2}\tilde{A}\tilde{D}^{-1/2}H^{(l)}W^{(l)}\right) \tag{1}$$

where $H^{(l)}$ is the matrix of node features at layer l, σ is an activation function, $\tilde{A} = A + I_N$ is the adjacency matrix with added self-loops through adding the identity matrix I_N, $\tilde{D}$ is the degree matrix of $\tilde{A}$, $W^{(l)}$ is the learnable weight matrix at layer l. This operation is performed iteratively across multiple layers, allowing the model to progressively refine node representations and incorporate complex relationships within the graph structure.

2) Model development

We developed two separate models, the GCN model and the baseline-LSTMs model, for classifying anomalies in CML and SoilNet datasets. Unique characteristics and availability of labels in each dataset determined the model architectures, with simplified versions presented in Fig. 2. To assess GCN effectiveness and benefits of incorporating the neighboring sensors information, we compare it with the baseline-LSTMs model, which lacks the GC layer and only uses one time series as input. All four models were implemented using Python 3.9.16 with TensorFlow and Keras API (2.11.1) and Spektral (1.3.0) libraries.

Preprocessed time series samples (see Section 3) in the forms of graphs or individual time series served as input to the models. The GNN model architecture (Fig. 2) starts with a GC layer, capturing spatial relationships between sensors, applied separately at each time step. The GC output is then concatenated to the original time series of flagged sensors. To ensure clarity in the explainability analysis, we refer to the input to the concatenation layer as the flagged sensor (FS) series and to the GC layer as a self-reference cycle or neighbor zero (N0).

Due to varying labeled sensors availability, the CML GCN predicts an anomaly probability for only one sensor of interest (graph classification problem), while the SoilNet GCN predicts scores for all sensors in the input graph (node classification problem). As a result, the CML version

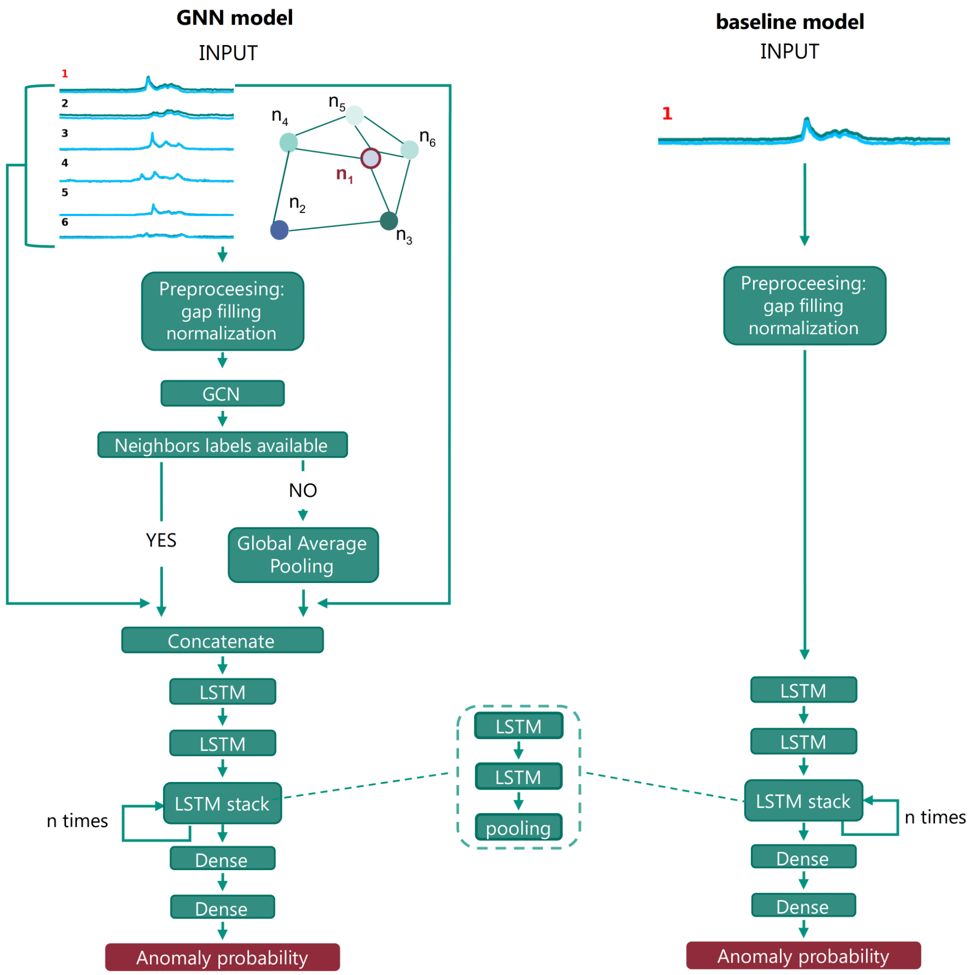

FIG. 2. Schematic representation of two anomaly detection models' architectures. On the left, the GCN model is depicted, incorporating GC for anomaly detection, while the right side depicts the baseline-LSTM without GC, illustrating the structural similarities and differences between the two approaches.

applies global average pooling, calculating mean values at each time step, to ensure consistent tensor shapes before concatenation. For SoilNet, where all neighbors were labeled, this step was not necessary. Given that GC operates independently at each time step, the model incorporates LSTM stacks to capture time dependencies. These stacks comprise LSTM layers combined with average pooling layers to downsample feature maps and reduce their size. The model concludes with dense layers allowing the network to extract high-level features, reduce the output dimension, and together with LSTM layers learn non-linear relationships.

Eventually, the network was trained utilizing the Adam optimizer and employing binary cross-entropy as the loss function. Model hyperparameters were tuned using manual search, adjusting parameters such as batch size, epochs, data normalization, learning rate, number of LSTM stacks, and units, as well as activation functions for each GC, dense, and LSTM layers. The full list of tuned hyperparameters is available in Tab. A1 in the Appendix.

c. Feature attribution through integrated gradients

We showcase the potential of feature attribution for QC by applying an XAI technique called the integrated gradients (IG) method to the GCN model and present results for the two selected CML examples. The interpretation of data-driven models by visualization of the feature attribution provides insight into the impact of certain input features on the model output. The methodology was developed by Sundararajan et al. (2017) and is often applied to image analysis, but can be seamlessly transferred to time series (classification) problems (Assaf and Schumann 2019; Jiang et al. 2022; Choi et al. 2022).

1) Theoretical background

The IG technique can be applied to a variety of integratable deep networks. As a post-hoc, model-agnostic interpretation methodology, the workflow comprises a series of model calls with altered input feature space. Thus, models within this category do not require further adaptation to be able to apply the methodology.

Similar to other gradient-based approaches such as Layer-wise Relevance Propagation (Bach et al. 2015), Deep Lift, (Shrikumar et al. 2017) or SmoothGrad (Smilkov et al. 2017), IG calculates the gradient of the input with respect to the model output. The method integrates gradients along different model inputs that represent intermediate steps from a linear interpolation between a user-defined feature baseline and the actual features (Sundararajan et al. 2017). The result represents an attribution of the model output to the individual input features.

Mathematically, the integrated gradients are the path integral from the baseline to the model input where the integrated gradient along the i^{th} dimension is defined as:

$$IG_i(x) ::= (x_i - x_i') \times \int_{a=0}^{1} \frac{\partial F(x' + a \times (x - x'))}{\partial x_i} d\alpha, \tag{2}$$

where x is the model input, x' is the baseline, $\frac{\partial F(x)}{\partial x_i}$ is the gradient of $F(x)$ along the i^{th} dimension and a is a scalar parameter ranging from 0 to 1, representing the interpolation factor between the baseline input and the actual input. The path integral can be approximated with the Riemann-Integral which is the sum of the gradients for sufficiently small steps. IG satisfies the completeness axiom so that the sum of the attributions of all features from one sample adds up to the difference between the output for the original model input and the baseline. It can be used as a sanity check and allows for qualitative comparison of attributions in a numeric sense (Sundararajan et al. 2017) which ultimately led us to choose this method for our work. Furthermore, it allows for a quantitative comparison of attributions among samples of different time steps.

2) Implementation

We applied the IG method to the CML dataset in order to interpret the model decisions and understand the contribution of features of the flagged time series in comparison to the features of the neighboring sensors which were processed by the GCN.

The model output at the baseline should represent a neutral state so that the prediction of the baseline is near zero (Sundararajan et al. 2017). We chose the baseline to be zero after investigating random and mean baselines. A random baseline introduced strong noise in the final attribution pattern while mean baselines led to smoothed attribution patterns with insufficient contrast.

The TensorFlow library was used to record the gradients through back-propagation and automatic differentiation (Samek et al. 2021). The gradients were retrieved for 100 interpolation steps and integrated using the Riemann-Integral (Sundararajan et al. 2017). After integration, the resulting attributions were visualized in the form of a heatmap on a sample basis (Section d).

When working with time series data, consecutive samples usually exhibit a substantial overlap across most of the sequence length. (Fig. 3). As a result, every heatmap generated from samples serves as a momentary depiction, and when combined into a video, viewers can track the changes in the attribution of a certain feature over time. These videos were created for the CML sensors and time series presented in this work and are available as supplementary material to the manuscript.

Our main goal lies in the understanding of the neighbors' contributions to the model output at different time steps compared to the influence of the flagged input time series FS. For a comprehensive evaluation of the whole time series, we aggregated (averaged) each sample-based heatmap along the sample time interval, resulting in one attribution value for each sensor at each timestep (Fig. 3).

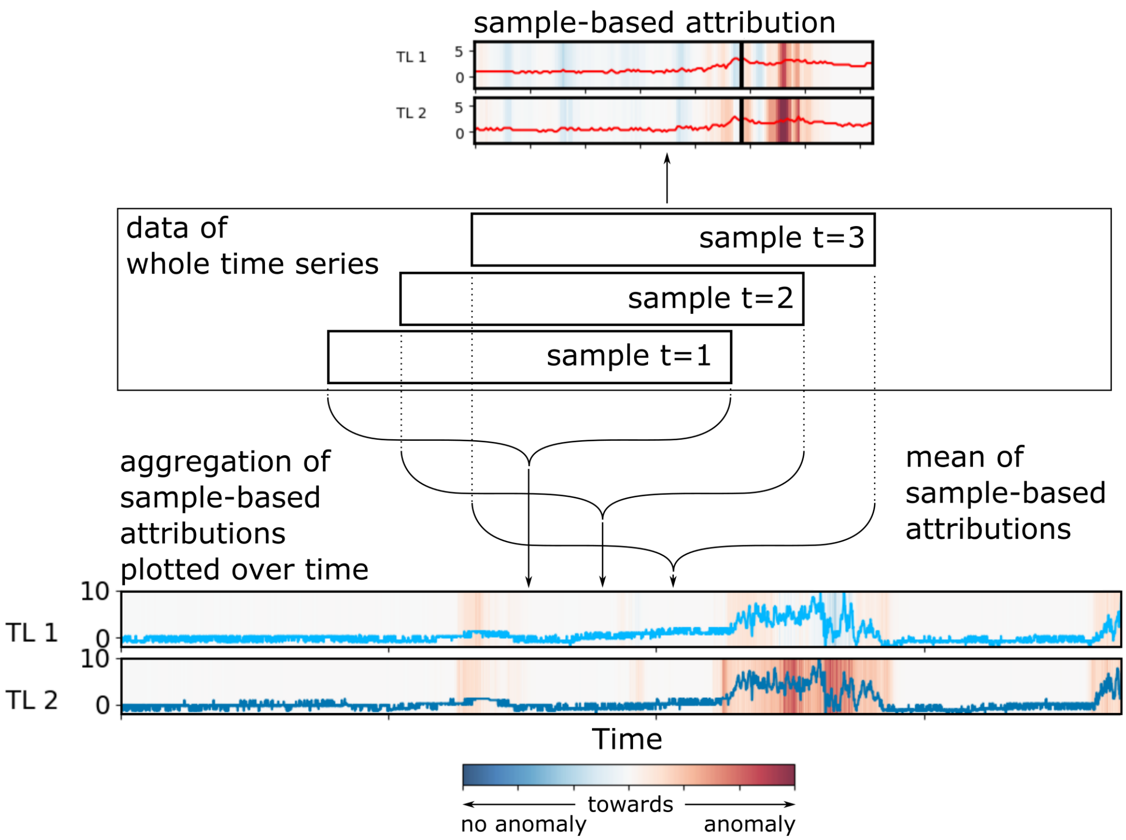

FIG. 3. Schematic view of the aggregation of the sample-based heatmaps to finally result in a time series of mean attributions. Each sample-based heatmap corresponds to the attribution of input features from a single model call, classifying an individual value within the original sensor data. The process involves concatenating numerous averaged sample-based attributions derived from temporally shifted input features, resulting in a comprehensive time series of mean attributions.

3. Model performance evaluation

After the development of anomaly detection models for the CML and SoilNet datasets, we evaluated them using key classification metrics covering different aspects. For this purpose, we used the receiver operating characteristic (ROC) curve and the Matthew's correlation coefficient (MCC).

The ROC curve is a commonly used graphical representation of the performance of a binary classification model. It depicts the trade-off between the true positive rate (TPR) and the false positive rate (FPR) for different discrimination thresholds determining the classification boundary between positive and negative classifications. The TPR represents the ratio of correctly classified positive observations to the total actual positives:

$$TPR = \frac{TP}{TP + FN}, \tag{3}$$

while FPR is the proportion of actual negative instances incorrectly identified as positive by the model:

$$FPR = \frac{FP}{FP + TN}. \tag{4}$$

Here, TP is true positives, TN is true negatives, FP is false positives, and FN is false negatives. TPR and FPR depend on the classification threshold which parameterizes the ROC curve depicting the model's ability to discriminate between positive and negative instances. In general, a steeper ROC curve indicates a better model performance. For a quantification of the performance shown in the ROC the area under curve (AUC) can be used. Its score ranges between 0 and 1 with 0.5 representing a random classification performance and higher values indicating better model performance.

The MCC is another widely used metric to evaluate binary classifiers and can be calculated using the following equation:

$$MCC = \frac{TP \times TN - FP \times FN}{\sqrt{(TP+FP)(TP+FN)(TN+FP)(TN+FN)}} \tag{5}$$

The equation results in values between -1, indicating total disagreement between prediction and true label, and 1, meaning perfect prediction, while the score of 0 denotes random guessing. The MCC takes into account all elements of the confusion matrix composed of TP, TN, FP, and FN and indicates a good performance only if there is a high accuracy for positive and negative classes. Therefore, it is extremely useful to evaluate the classification performance when the dataset is highly imbalanced.

Our evaluation procedure was comprehensive and covered several steps to provide a robust assessment of the models' performance. First, we conducted a 5-fold cross validation (CV) to analyze the potential sensitivity of the model to different data splits. Each dataset was partitioned

TABLE 1. Summary of AUC and MCC scores from final models, five runs of CV and their means, for both CML and SoilNet datasets. MCC scores are calculated based on the threshold obtained from the final model.

	CML				SoilNet			
	AUC		MCC		AUC		MCC	
	GCN	baseline-LSTM	GCN	baseline-LSTM	GCN	baseline-LSTM	GCN	baseline-LSTM
final	**0.974**	**0.880**	**0.683**	**0.306**	**0.859**	**0.782**	**0.462**	**0.345**
fold 1	0.949	0.898	0.399	0.125	0.843	0.806	0.468	0.347
fold 2	0.924	0.916	0.427	0.230	0.822	0.785	0.436	0.375
fold 3	0.942	0.861	0.518	0.231	0.860	0.814	0.468	0.391
fold 4	0.933	0.873	0.565	0.310	0.853	0.843	0.522	0.430
fold 5	0.955	0.876	0.588	0.238	0.909	0.833	0.551	0.513
mean	**0.941**	**0.885**	**0.445**	**0.257**	**0.858**	**0.816**	**0.477**	**0.394**

into five equal-sized subsets, and the models were iteratively trained five times, using four subsets (80%) for training and one (20%) for validation in each iteration resulting in five different models trained.

Following CV, we proceeded to train the final models using data split into training, validation, and test datasets in a 6:2:2 ratio, with equally sized temporal blocks for each split. Throughout the training process, we monitored the loss function on the validation dataset, and upon completion, assessed the model performance on the independent test dataset using the model with the lowest recorded validation loss. To establish anomaly flags for predictions, we carefully selected thresholds for all models (CV and final) that maximized the MCC scores on the validation dataset for the final models. Eventually, we conclude our evaluation with aggregated statistics with regard to the individual sensors.

4. Results

a. Cross-validation

Figure 4 presents the ROC curves of each of the 5 CV folds together with the mean value for both, GCN and baseline-LSTM models. For both, the CML and SoilNet datasets, there is a clear superiority of the GCN over the baseline-LSTM. The mean GCN ROC curves are consistently located to the left of the baseline models' curves, indicating a higher TPR for the same FPR. However, the CML GCN and baseline-LSTM exhibit significantly better performance than the

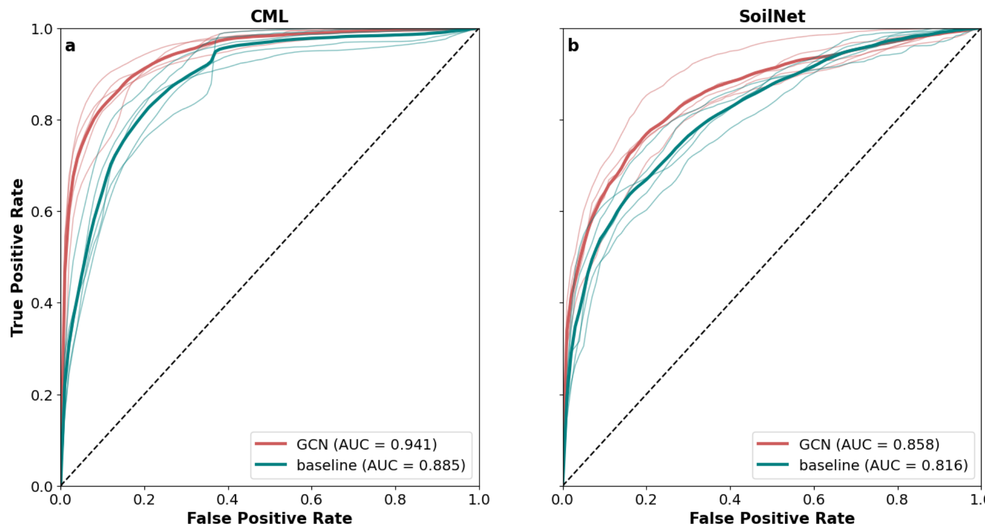

FIG. 4. ROC curves comparing the performance of GCN (red) and baseline-LSTM models (green) in 5-fold CV. The bold lines represent the mean performance, while the thin lines illustrate individual runs. Panel (a) corresponds to CML data, and panel (b) displays results for the SoilNet.

SoilNet models, as indicated by their closer proximity to the upper-left corner of the plot and an average increase in AUC scores of approximately 0.08. Also, for CML most of the GCN folds performed better than any other baseline-LSTM model runs while for SoilNet individual GCN and baseline runs overlap with each other.

As summarized in Table 1, the CML AUC scores for GCN ranged between 0.924 and 0.955, with a mean of 0.941, while for the baseline-LSTM, the AUC varied from 0.861 to 0.916, resulting in a mean of 0.885. For SoilNet, AUC values were smaller than for CML, ranging between 0.822 and 0.909 for GCN, with a mean of 0.858, and between 0.785 and 0.843 for the baseline-LSTM, with a mean of 0.816.

The same table also presents the MCC scores, which were consistently higher for the GCN models in both datasets. To calculate the MCC scores, it was necessary to determine the classification thresholds. Following the procedure described in Section 3, for the CML dataset, we established thresholds of 0.956 and 0.044 for the GCN and baseline-LSTM, respectively. Similarly, for SoilNet, the corresponding thresholds were 0.814 and 0.640. For CML, the maximum MCC achieved by GCN was 0.588, compared to 0.310 for the baseline-LSTM. Similarly, for SoilNet, the maximum

MCC reached 0.551 for GCN, while for the baseline-LSTM, it was higher than that achieved on the CML data, reaching 0.513.

b. Final model evaluation: visual and statistical analysis

FIG. 5. Classification results of CML and SoilNet time series data from selected sensors. The upper panel in each subplot displays the original TL time series for CML and moisture and battery voltage for SoilNet. The panels below showcase the classification outcomes for the GCN and the baseline-LSTM, respectively, with distinct colors representing the four classes derived from the confusion matrix, as well as no data (see Sec. 3) and samples with automatic flags. The red vertical line in (b) points out to the event described in XAI analysis (Section d).

We proceeded with the evaluation of the models' performance through visual analysis of the original time series together with the classification results for the final baseline-LSTM and GCN models. All presented results are based on the test data split. Fig. 5 illustrates examples of classified time series using the GCN and baseline-LSTM models with panels a and b for CML and c and d for SoilNet. For the CML examples, both models effectively captured the majority of anomalies, however, the GCN model exhibited greater accuracy.

Fig. 5a depicts three anomaly events with signal fluctuations of up to 10 dB, each of them lasting for approximately 9 hours. Both models struggled with the correct classification of the first event and performed similarly on the second and third. However, the baseline-LSTM showed a high amount of false positives such as on July 17th and July 19th, while the GCN showed a high accuracy in these periods. Fig. 5b shows a similar picture with a time series covering two anomalous CML events and one rain event (intended measurement) between 18 UTC on July 28th and 6 UTC on July 29th. The first anomaly lasted 11 hours displaying a jagged shape, while the second, shorter event lasted 5 hours featuring a sharp trough. Although both events were detected, the onset of the first event was delayed. The GCN performed better in detecting the anomalies (more TP) and, at the same time recognized the rain event as a non-anomalous pattern while the baseline-LSTM faced challenges primarily related to false positives.

In both examples for the SoilNet dataset presented in Fig. 5c and d, prolonged periods are labeled as 'no data' due to missing periods longer than our maximum interpolation length. Consequently, data samples with a length of 84 hours, which form the input, contained missing values and had to be excluded from the analysis. The first SoilNet example (Fig. 5c) displays an anomalous soil moisture time series including several automatic anomaly flags. The first analyzed period, between October 14th and 20th, exhibits a constant battery voltage (blue line) of around 3.2 V and a relatively steady moisture level of around 39% (teal line), with a few minor drops. During the second period, from October 24th to 28th, the battery level decreases slightly and fluctuates, while more noticeable fluctuations are visible in moisture, which decreases slightly towards the end of the series. Both the GCN and baseline-LSTM struggled to accurately predict the start and end of the first event, identifying only the central part as anomalous. Here, the baseline-LSTM outperformed the GCN by detecting the longer anomaly period. In the second period, where the moisture anomaly was clearer, both models correctly classified the onset of the anomaly. Nevertheless, the baseline-LSTM failed to detect the second half of the event and erroneously identified an anomaly on October 9th, resulting in an FP detection.

The second analyzed time series presented in Fig. 5d contains four anomalous events. The battery voltage values show a strong diurnal cycle throughout the entire time series. The GCN showed superior performance for the first and second periods characterized by notable bumps and a gradual decrease in moisture afterward. However, for the third period, where the moisture anomaly was less obvious and manifested only as a steady decline, and the last event registered as a sharp peak, the baseline-LSTM performed better. In summary, while the GCN model applied to the SoilNet time series demonstrated only a slight advantage over the baseline-LSTM, the quantitative statistics presented below paint a different picture, particularly when more non-anomalous periods are included in the analyzed data.

A quantitative analysis using the final models on the entire test dataset confirms the advantages of incorporating neighboring information (Table 1). Specifically, for the CML dataset, the GCN model achieved an AUC of 0.974 and MCC of 0.683, outperforming the baseline-LSTM (AUC: 0.880, MCC: 0.306). For SoilNet, although scores were lower, the GCN model still outperformed the baseline-LSTM, with AUC at 0.859 and MCC at 0.462. However, it is important to note that MCC is a threshold-dependent score, influencing its interpretation. To gain insights into how different thresholds impact performance, we calculated FPR and TPR rates for the chosen thresholds. For GCN, FPR and TPR reached 0.230 and 0.966, respectively, compared to 0.166 and 0.825 for the baseline-LSTM. For SoilNet, GCN demonstrated a lower FPR (0.095) than the baseline-LSTM (0.123) and a higher TPR (0.597) compared to the baseline-LSTM (0.541). These results underscore the benefits of leveraging neighboring information in improving the overall predictive performance of the GCN model.

c. Classification performance for individual sensors

We aggregated the results and computed metrics separately for each sensor to evaluate the consistency of prediction skills. The top panels in Fig. 6 present the scatter plots of AUC values of baseline-LSTM and GCN models for the CML and SoilNet datasets.

In the CML dataset (Fig. 6a), all points lie on the right side of the diagonal, indicating GCN's superiority. Most sensors show a GCN AUC score approximately 0.1 higher than the baseline-

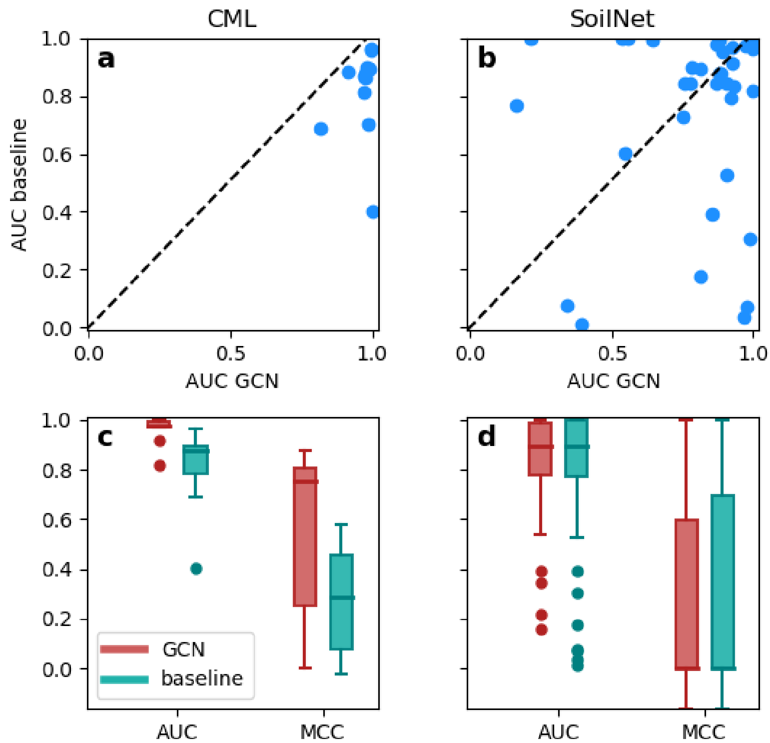

FIG. 6. Scatter plots (upper panels) and box plots (bottom panels) illustrating the model performance metrics for baseline-LSTM and GCN models on CML (left panels) and SoilNet (right panels) datasets. Each data point in scatter plots reflects the AUC score for a specific sensor, while box plots depict the distribution of AUC scores and MCC values on the left and right sides of each panel, respectively. The GCN outcomes are presented in red, while the baseline-LSTM results are shown in teal.

LSTM, with an exception where GCN achieved nearly 1 compared to 0.40 for the baseline-LSTM. This trend is confirmed by the box plots in Fig. 6c, where GCN AUC median value is almost 1, while the baseline-LSTM drops slightly below 0.9. The GCN demonstrates a negligible interquartile range, with two outliers at 0.80 and 0.90, while the baseline-LSTM has one outlier, resulting from a wider box spreading between slightly over 0.75 and 0.90. For MCC, the GCN model performed better, with a median of 0.75 compared to 0.30 for the baseline-LSTM, although MCC scores varied substantially across sensors.

Results for the SoilNet dataset (Fig. 6b and d) exhibit more heterogeneity. The scatter plot (Fig. 6b) shows points concentrated in the upper right corner, indicating comparable model performance. While for most instances the GCN model outperformed the baseline-LSTM, there were also cases where GCN failed and performed below random prediction, indicated by AUC scores below 0.5. This varied performance is reflected in the box plots (Fig. 6d), where the median AUC and MCC scores for both models were identical, measuring 0.89 and 0, respectively. Nevertheless, the AUC interquartile range for the baseline-LSTM is slightly larger, with six outliers, while the GCN had four outliers with a minimum AUC of 0.16. The boxes for MCC extend from 0 up to 0.60 and 0.76 for baseline-LSTM and GCN models, respectively, with long whiskers reaching up to 1, indicating significant variability in individual sensors performance.

d. Sample-based feature attribution

The attribution values of all model's input features, that is the normalized time series values of the flagged sensor and its neighbors, are visualized as a heatmap with colors ranging from blue (negative) over white (zero) to red (positive). Negative attribution values lead the model output towards zero (no anomaly). Conversely, positive attributions guide the model output towards one (anomaly). Fig. 7 depicts the heatmap for CML time series presented in Fig. 5b at 00:40 UTC on 29th of July, 2019 where four representative neighbors out of 21 were selected for demonstration. The complete figure is provided in the Appendix (Fig. C2). The features of the flagged time series were not subject to the GC process and obtained remarkably higher attribution than the neighbors and the self-reference cycle so we scaled the attribution of the neighbors and self-reference cycle by a factor of 25 for visualization purposes.

The upper panel in Fig. 7 illustrates the flagged time series, indicating the onset of a rain event around time step 115. The integrated gradients analysis shows a positive attribution for the flagged sensor, leading to an increase in the model's prediction towards one and triggering an anomaly classification. However, similar rain events with comparable shapes occur at neighboring sensors N4 and N11, and approximately 40 timesteps earlier at sensor N15. These neighboring sensors receive negative attribution, resulting in a decrease in the model output and suggesting no anomaly. This influence ultimately leads the model decision away from an FP classification but instead towards a TN classification. Consequently, the model has learned that when certain patterns observed in the flagged time series also appear at neighboring sensors, the likelihood of an anomaly is reduced, indicating that a rain event might be responsible for the increase in sensor readings. The neighboring information is missing in the baseline-LSTM, thus the discussed event is misclassified in the prediction of the baseline-LSTM (Fig. 5b).

e. Sample-aggregated attributions over time

In Fig. 8 we present the averaged sample-aggregated attributions of each time step plotted over time from the first sensor shown in Fig. 5a). The aggregation is performed by averaging the attributions of each sample along the time dimension as indicated in Fig. 3.

Similar to the significance of neighboring sensors discussed in Section d, comparable importance of neighbors can be observed in two instances of TN events with high model predictions in this time series. For the first TN event (event 1), the self-reference cycle N0 and the neighbor N3 showed a similar pattern in the TL record as the flagged sensor but received negative attribution, thus leading away from a False Positive classification. The second TN event appears later (event 4) where sensors N0, N4, N5, N6, and N7 show comparable TL records as the flagged sensors, hence showing negative attribution and avoiding a misclassification here as well. The baseline-LSTM fails to correctly classify these events (Fig. 5a), demonstrating a clear advantage of the GCN model over the baseline-LSTM. In general, the positive attribution mainly accumulates along the flagged time series while the self-reference cycle N0 and the other neighbors were predominantly attributed with negative values. Exceptionally strong negative attribution can be observed during the first anomaly event (event 2). The self-reference cycle and presumably similar patterns at the neighboring sensors N1, N3, and N4 cause a model prediction drop in the middle of the anomaly event leading to FN classifications. For the 3rd and 4th events, the self-reference cycle also shows a negative attribution, but in the absence of a clear signal from the neighboring sensors, this sums to only a small negative attribution overall. Thus, the positive attribution of the flagged time series leads the majority of the event towards a TP classification. Here, the IG method reveals that in some cases the model can put too much attention on fluctuations in the neighboring sensor signals even though the flagged time series shows a pattern that would not be classified as a rain event by an expert. The same plot for the sensor shown in Fig. 5b) is provided in the appendix (Fig. C1).

5. Discussion

Our research explores the application of GCNs for anomaly detection in two diverse environmental datasets: CML and SoilNet. Despite differences in spatial and temporal resolution, both datasets feature irregularly and sparsely distributed environmental sensors across their respective regions. Employing GCNs allowed us to leverage information from neighboring sensors through message passing, enhancing anomaly detection compared to baseline-LSTMs that do not employ GC. This study is the first to demonstrate the merits of GCNs in detecting anomalies in real-world environmental sensor data, while previous research primarily focused on synthetic or benchmark datasets commonly used in artificial intelligence (AI) applications. Furthermore, existing QC frameworks for environmental sensor data typically classify individual sensors using established methods such as ARIMA, SVM, and convolution neural network (CNN) models, neglecting the potential benefits of incorporating neighbor information.

Our robust evaluation, employing 5-fold CV, consistently demonstrated superior scores for the GCNs over the baseline-LSTM, illustrating the benefits of incorporating neighbor information in anomaly detection. The added benefit was more pronounced for CML than for SoilNet data.

The higher performance scores on the CML dataset may be attributed to the robust and precise labeling strategy and better data quality in general. CML data underwent meticulous examination by four independent experts and merged into reliable anomaly labels by majority vote. In contrast, for SoilNet, flagging was performed by different experts leading to potential inconsistencies. The flags we used included both clearly erroneous data and suspicious periods where automated tests had already flagged many data points, indicating for example low battery voltage. Consequently, there were instances where flagging was not executed with high temporal precision leading to valid observations being erroneously labeled as anomalies, thus introducing incorrect information into the model. Soil moisture observations exhibit strong variability at a small scale and sensitivity to numerous factors (Mittelbach et al. 2012; SU et al. 2014). Both lead to diverse signal fluctuations and disturbances and, consequently, to a large intra-class variability for the anomaly and no-anomaly classes that impacted the detection accuracy. Moreover, automatic flags, easily detectable and subsequently excluded in our study, resulted in reduced available samples and graph nodes, also influencing model performance.

This work emphasizes the power of explainable artificial intelligence (XAI) in interpreting model predictions and showcases the importance of neighbors for the GCN CML model prediction. This is achieved by utilizing interpretable attributions derived from integrated gradients of the input features. Through sample-based and aggregated attribution heatmaps, we illustrated to which degree information from neighboring sensors influenced the final classification outcome. During rain events, where the baseline-LSTM erroneously flagged anomalies, the GCN model accurately identified the rain event by recognizing similar sensor reading patterns across neighboring sensors. This highlights the essential role of neighboring sensors in informing the model and aiding in the distinction between rain events and anomalies. However, if an anomaly event identified by experts coincides with signal fluctuations at other sensors, it may lead to a decrease in model accuracy.

While our study offers valuable insights, it also has limitations. We worked with a limited three-month CML dataset, analyzing data from only 20 out of 3904 sensors that underwent manual quality checks, which resulted in unlabelled neighbors within the graph. To address this, we applied global pooling after GC, smoothing artifacts present only in particular neighbor signals. Additionally, our approach did not consider sensor correlations in establishing graph links, relying solely on experimentally chosen distances, which may affect model performance. Lastly, during the data preparation phase, we employed simple linear interpolation to fill up short data gaps. However, longer gaps remained, resulting in a reduced number of samples, which was particularly noticeable in the SoilNet dataset due to the frequent occurrence of such gaps. While these limitations do not weaken our claim that GCNs performed superior in this study, it is important to acknowledge that even better model performance could potentially be achieved. However, overcoming these limitations poses challenges, as manual labeling efforts are extensive, and addressing data gaps would require sophisticated infilling methods that are yet to be developed.

6. Conclusions

This study demonstrates the potential of Graph Neural Network (GNN) for improving automated quality control (QC) of environmental sensor networks. The superior performance of GCN models, as shown across both datasets, highlights the significance of incorporating spatial context into anomaly detection tasks. The visualization of the feature attribution confirms the importance of information from neighboring sensors and can support experts in understanding the AI-model behavior when discriminating anomalies from valuable observations like rain events in the case of CML data. We found that the GCN consistently achieved higher evaluation metrics than the baseline-LSTM model. For CML, the AUC for GCN was notably higher at 0.974 compared to 0.880 for the baseline-LSTM, accompanied by MCC scores of 0.683 (GCN) and 0.306 (baseline-LSTM). Conversely, SoilNet demonstrated lower performance, with GCN achieving an AUC of 0.859 and the baseline-LSTM at 0.782. Correspondingly, GCN attained an MCC score of 0.462 compared to 0.345 for the baseline-LSTM.

Visual inspection of flagged time series demonstrated the clear superiority of the GCN over the baseline-LSTM model which proved to be proficient at classifying anomalies and resilient against events often misidentified by the baseline-LSTM. However, this advantage of GCN was less evident for SoilNet than for the CML data. We found a consistent performance across CML sensors, while there was a notable variation across SoilNet sensors. The CV results showed that, while using a comparatively low amount of flagged data, robust performance can be achieved and an automated QC of much larger amounts of data becomes feasible. Comparing the results of the two datasets leads to the hypothesis that more carefully flagged data requiring multiple experts to agree on a label can enhance the performance of the proposed algorithm which may be tested in future research. The same holds for the performance scaling with an increased amount of training data which should be considered for the operationalization of such an approach.

Acknowledgments. Elżbieta Lasota was funded by the Helmholtz AI project RESEAD from the Initiative and Networking Fund of the Helmholtz Association (grant no. ZT-I-PF-5-148), Julius Polz by the German Research Foundation (grant no. CH 1785/1-2, RealPEP), Luca Glawion by the Helmholtz-Innopool project SCENIC, and Lennart Schmidt by the Federal Ministry of Education and Research of Germany (BMBF, grant no. 02WDG1641B, i-SEWER project). We thank the Helmholtz Association for setting up the Helmholtz.AI initiative that initially brought together the authors of this work. Also, we thank the Helmholtz Association and the Federal Ministry of Education and Research (BMBF) for supporting the DataHub Initiative of the Research Field Earth and Environment. The DataHub enables an overarching and comprehensive research data management, following FAIR principles, for all Topics in the Program Changing Earth – Sustaining our Future. XAI analyses were conducted at the HPC Cluster EVE, jointly operated by the Helmholtz Centre for Environmental Research - UFZ and the German Centre for Integrative

Biodiversity Research Halle-Jena-Leipzig. We appreciate Mohit Anand's feedback on the IG methodology. The Hohes Holz observatories are supported by TERENO, funded by the Helmholtz Association and the Federal Ministry of Education and Research (BMBF). We acknowledge all experts involved in manual QC, especially Corinna Rebmann, Juliane Mai, and Matthias Cuntz, for providing labeled SoilNet data. We thank Ericsson Germany for supporting the acquisition of CML data.

Data availability statement. The CML data supporting this research was provided to the authors by Ericsson. This data is not publicly available as Ericsson restricted the distribution of this data due to their commercial interest. In order to obtain CML data for research purposes a separate and individual agreement with the network provider has to be established.

The SoilNet data used in this study is available upon request at `https://www.ufz.de/record/dmp/logger/806/en/`.

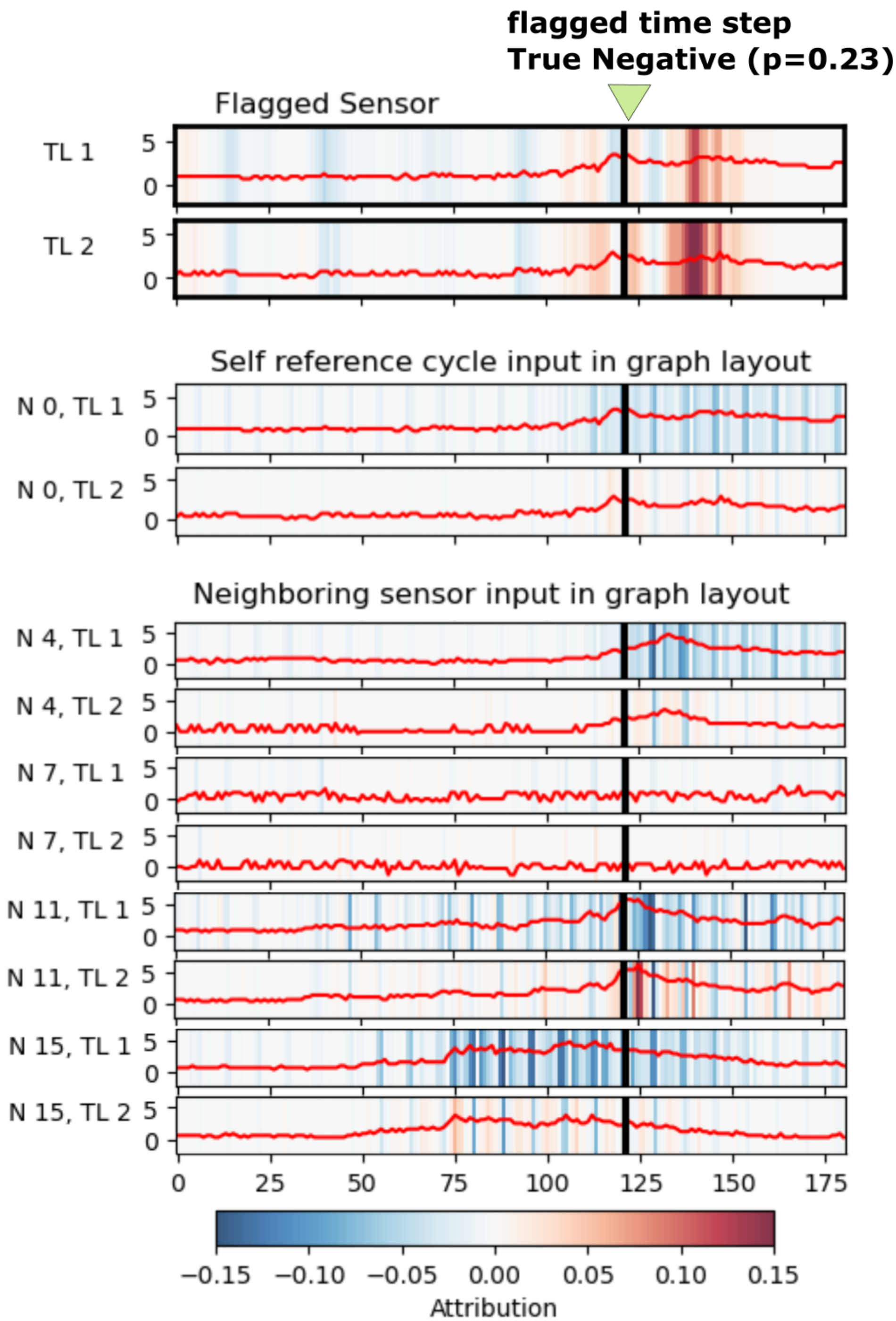

FIG. 7. Sample-based attribution heatmap for CML sensor (Fig. 5b) at 00:40 UTC on 29th of July, 2019. Input feature time series TL1 and TL2 from the flagged sensor, the self-reference cycle, and its neighbors are plotted over the sampling time interval. The background color indicates the IG attribution of each feature. The attribution of the self-reference cycle and the neighboring sensor inputs are scaled by a factor of 25 for visualization purposes.

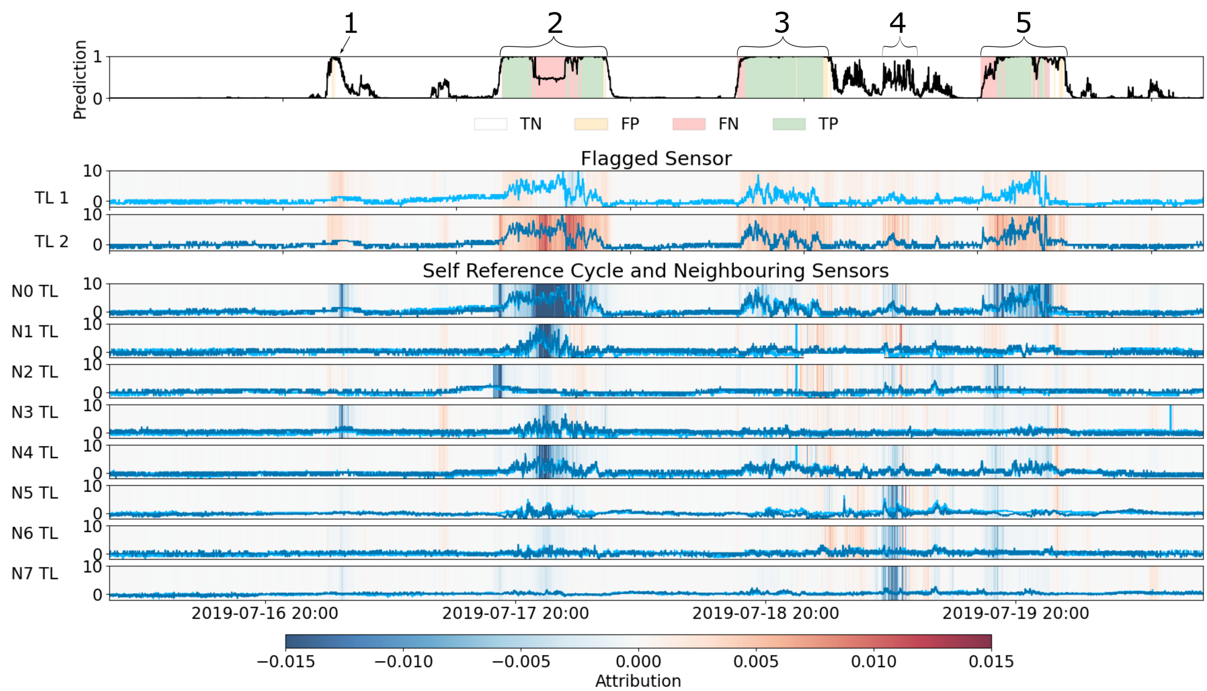

FIG. 8. Aggregated attribution for each sample plotted over time for the CML sensor depicted in Fig. 5a. Each sample-based heatmap was averaged across the sample time interval (181 minutes) to finally obtain one value for each time series per sample. The top panel depicts the model prediction and the resulting classification with the numbers above indicating the analyzed event number. The second and third panels show the time series of the flagged sensor and the corresponding aggregated attribution, separately for channels TL1 and TL2. The time series of the other panels show the model input of the self-reference cycle and neighbors. The color in the background indicates the aggregated attribution of that respective time step averaged across channels TL1 and TL2. The attribution of the neighbors and self-reference cycle was scaled with a factor of 25 for visualization purposes.

APPENDIX A

Hyperparameters used in model development

Table A1 lists the final set of hyperparameters employed during the training of the models for anomaly detection in the CML and SoilNet datasets.

TABLE A1. Hyperparameters used in model training for CML and SoilNet datasets. This table lists the final set of hyperparameters employed during the training of the models for anomaly detection in the CML and SoilNet datasets.

	CML		SoilNet	
	GCN	**baseline-LSTM**	**GCN**	**baseline-LSTM**
data normalization	rolling median removal		min-max scaler	
time series length (before+after)	120 + 60 minutes		72 + 12 hours	
edge formation criteria	distance<=10 km		distance<=30 m and depth difference=0 or distance=0 and depth difference<=0.1 m	
GCN:				
layer	GeneralConv	GeneralConv	GeneralConv	GeneralConv
channels	16	-	16	-
activation	PReLU	PReLU	PReLU	PReLU
LSTM:				
units	16	16	16	16
stack numb	2	2	2	2
max pooling size	3	3	3	3
dense:				
units	64	64	64	64
activation	leaky ReLU	leaky ReLU	leaky ReLU	leaky ReLU
epochs	20	20	40	40
batch size	128	128	32	32
learning rate	0.0005	0.0005	0.0001	0.0001

APPENDIX B

Time series comparison of classified and neighboring sensors

This appendix provides a visual comparison of the classified acCML and SoilNet sensors' data described in detail in Section b with the data from the neighboring sensors.

APPENDIX C

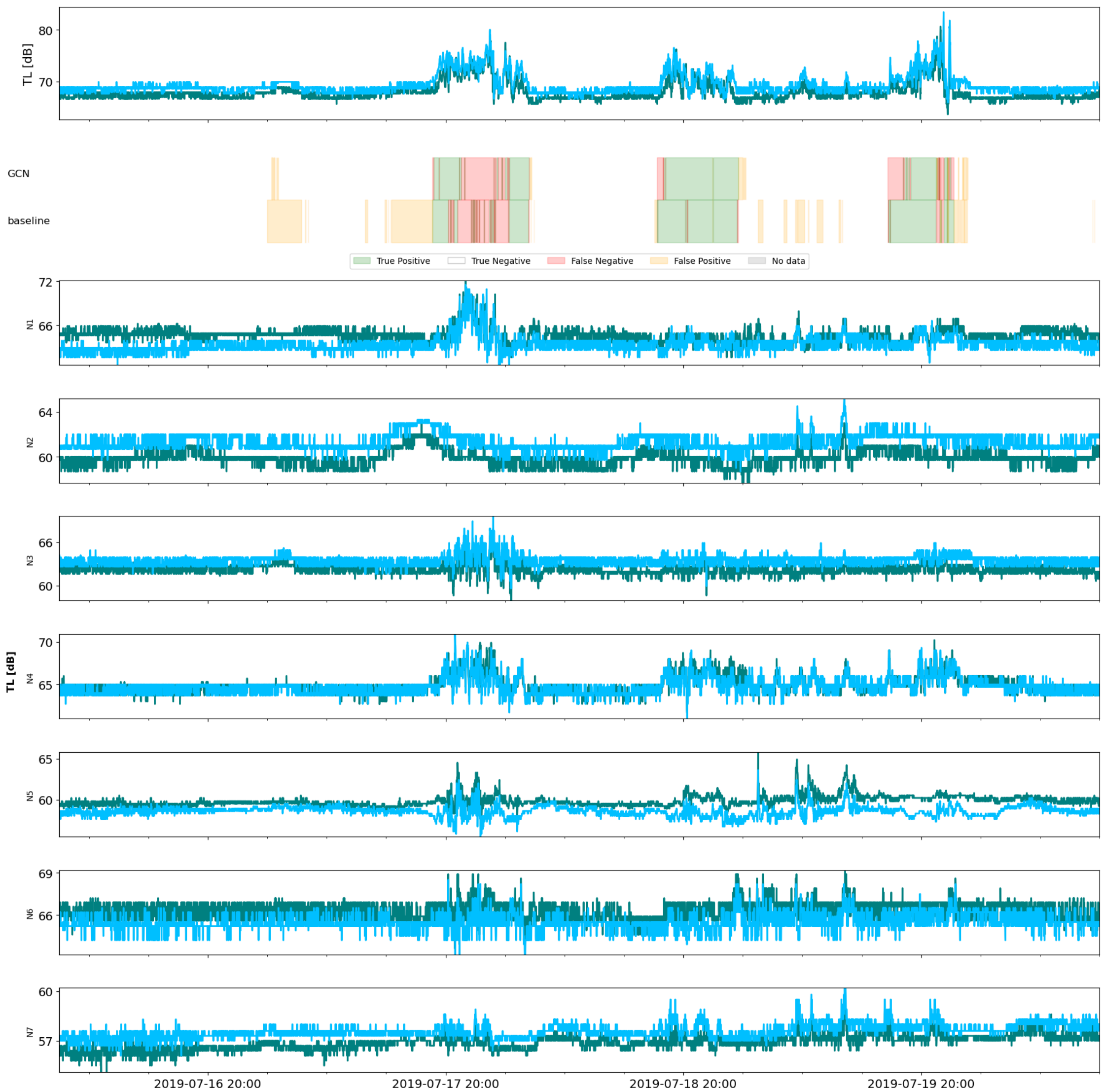

FIG. B1. Flagged CML time series with neighboring sensors and anomaly detection results. The uppermost panel presents the flagged CML time series, previously depicted in Fig. 5a, with additional panels below illustrating the time series of neighboring sensors. The color indicates the confusion matrix results of anomaly detection.

Additional figures of integrated gradients attributions

This appendix provides the complete version of the sample-based attribution from Fig. 7 and a figure of aggregated sample attributions from the other sensor.

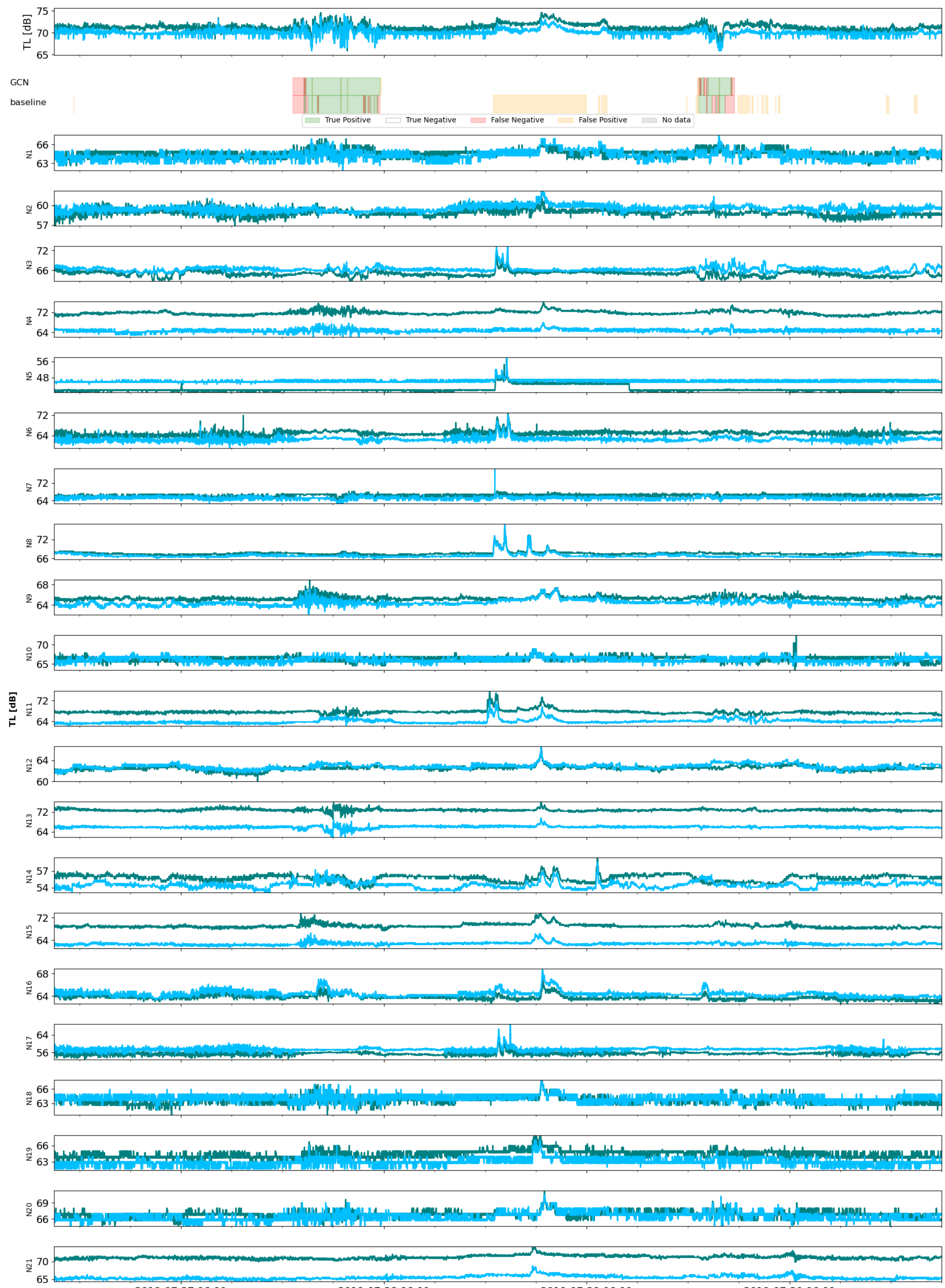

FIG. B2. Same as Fig. B1 but for the CML sensor depicted in Fig. 5b

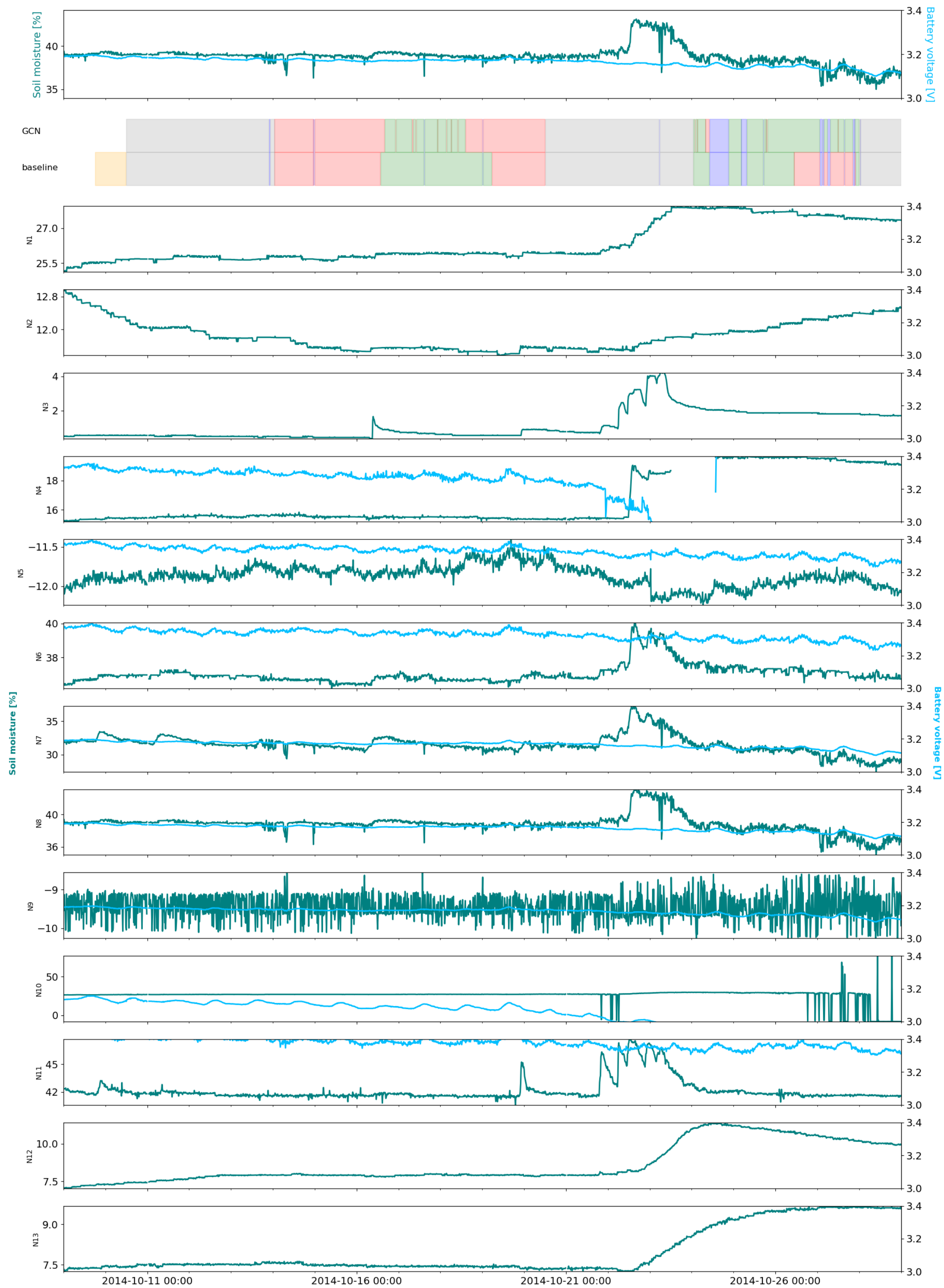

673 Fig. B3. Flagged SoilNet time series with neighboring sensors and anomaly detection results. The uppermost panel presents the flagged SoilNet time series, previously depicted in Fig. 5c, with additional panels below illustrating the time series of neighboring sensors. The color indicates the confusion matrix results of anomaly detection, as well as no data and samples with automatic flags.

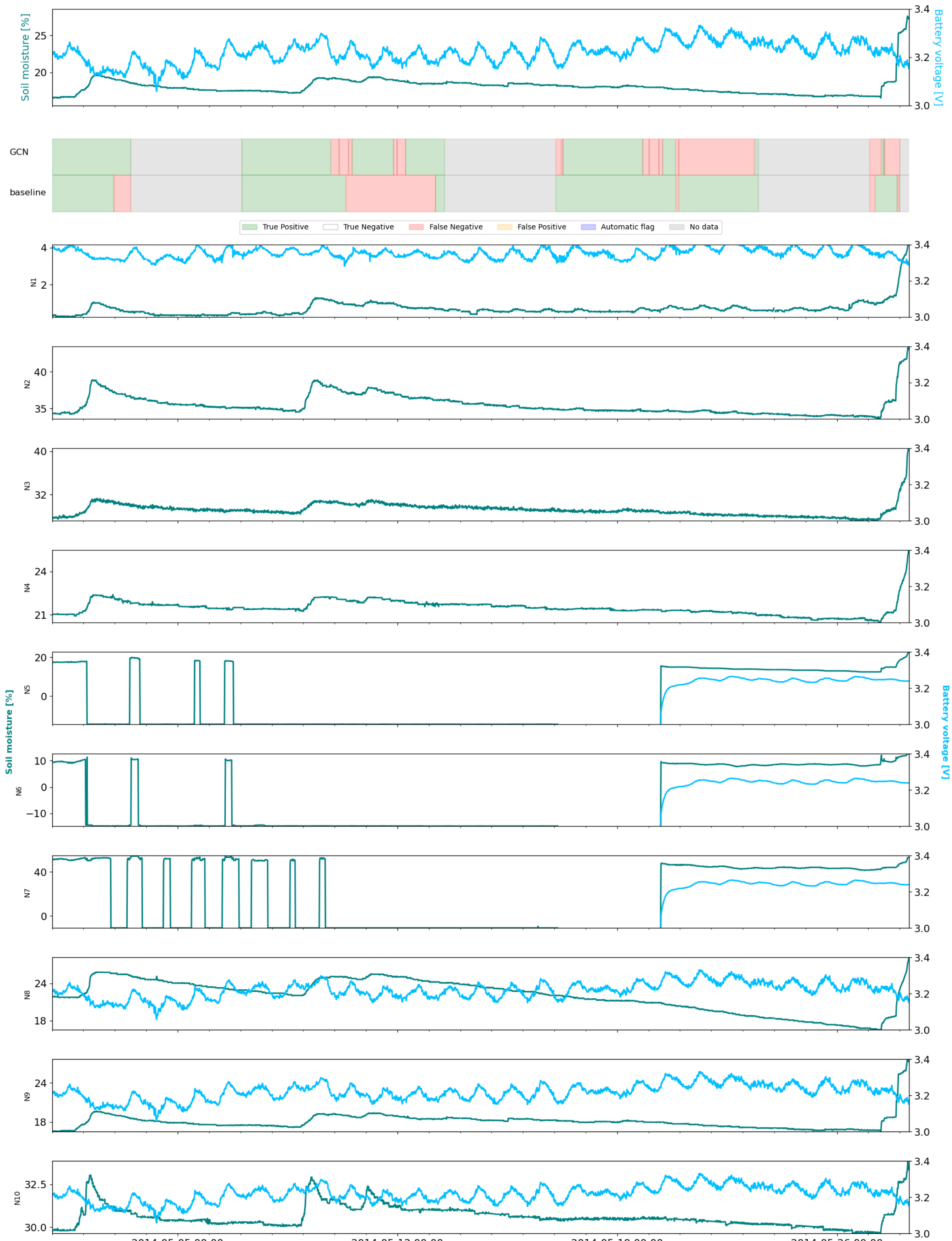

FIG. B4. Same as Fig. B3 but for the SoilNet sensor depicted in Fig. 5d

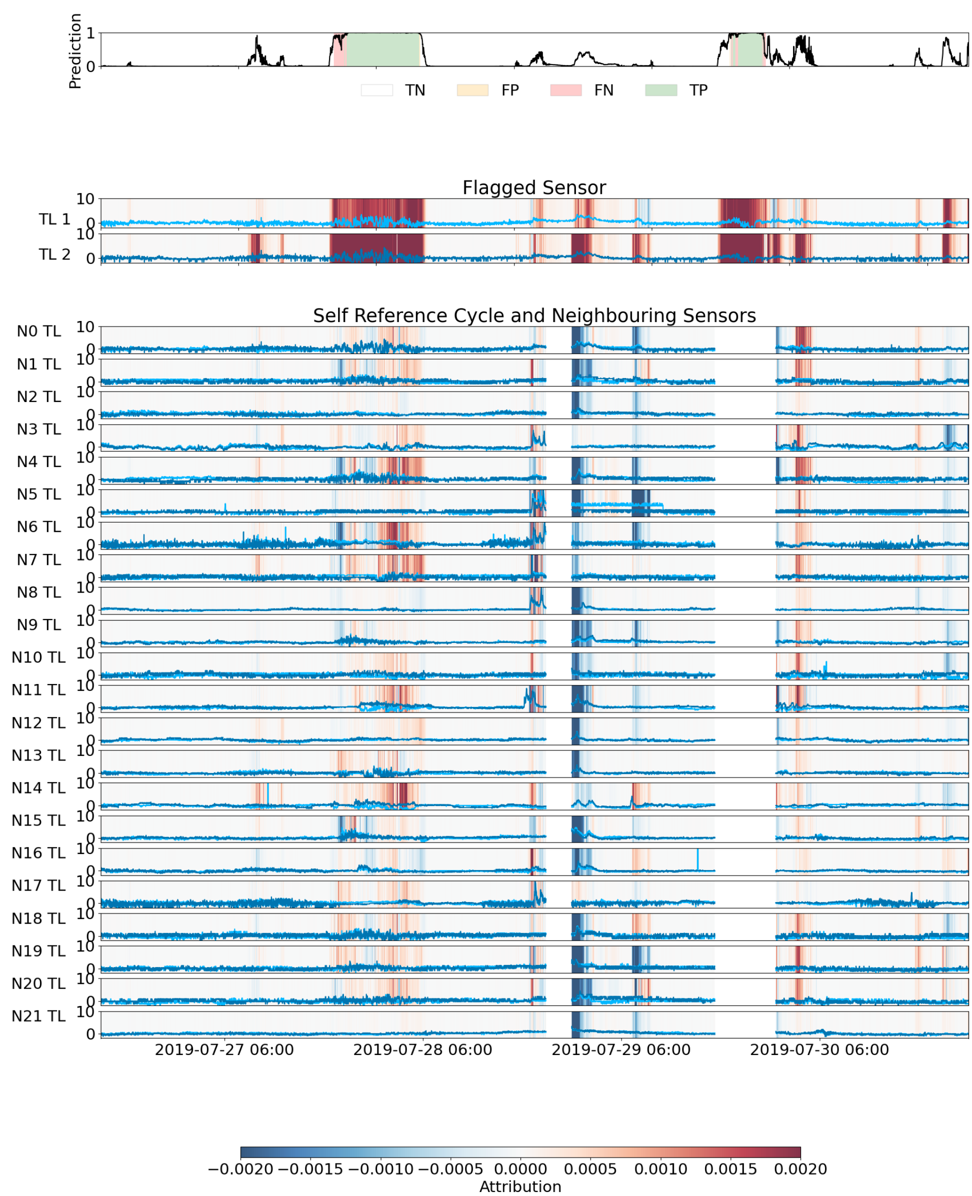

FIG. C1. Similar figure as Fig. 8 but for the other sensor.

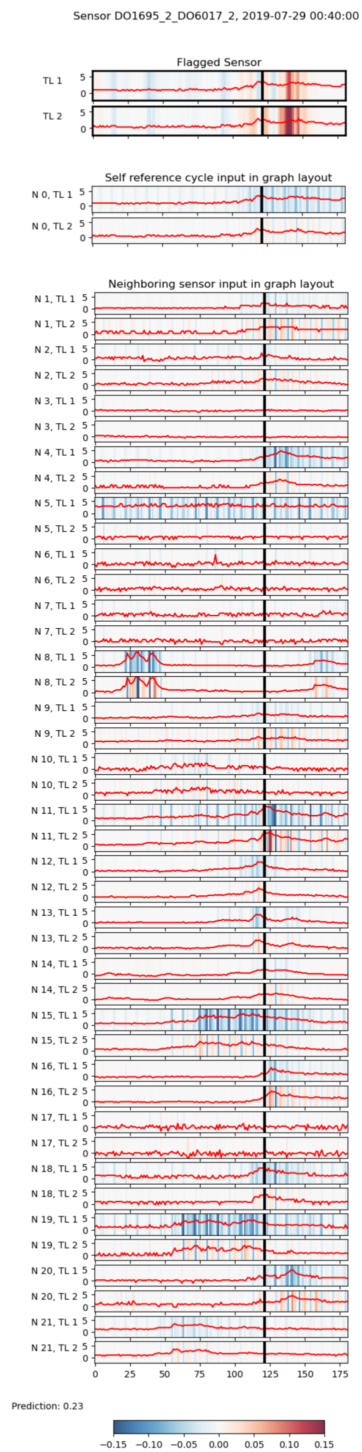

FIG. C2. Complete version of Fig. 7 including all neighboring sensors and their Integrated Gradient attributions.

References

Agarwal, C., M. Zitnik, and H. Lakkaraju, 2022: Probing gnn explainers: A rigorous theoretical and empirical analysis of gnn explanation methods. *International Conference on Artificial Intelligence and Statistics*, PMLR, 8969–8996.

Assaf, R., and A. Schumann, 2019: Explainable deep neural networks for multivariate time series predictions. *IJCAI*, Macao, 6488–6490, https://doi.org/10.24963/ijcai.2019/932.

Atlas, D., and C. W. Ulbrich, 1977: Path- and Area-Integrated Rainfall Measurement by Microwave Attenuation in the 1–3 cm Band. *Journal of Applied Meteorology and Climatology*, **16 (12)**, 1322–1331, https://doi.org/10.1175/1520-0450(1977)016⟨1322:PAAIRM⟩2.0.CO;2.

Bach, S., A. Binder, G. Montavon, F. Klauschen, K.-R. Müller, and W. Samek, 2015: On pixel-wise explanations for non-linear classifier decisions by layer-wise relevance propagation. *PloS one*, **10 (7)**, e0130 140, https://doi.org/10.1371/journal.pone.0130140.

Baldassarre, F., and H. Azizpour, 2019: Explainability techniques for graph convolutional networks. *arXiv preprint arXiv:1905.13686*.

Bogena, H., M. Herbst, J. Huisman, U. Rosenbaum, A. Weuthen, and H. Vereecken, 2010: Potential of wireless sensor networks for measuring soil water content variability. *Vadose Zone Journal*, **9 (4)**, 1002–1013, https://doi.org/https://doi.org/10.2136/vzj2009.0173.

Bogena, H. R., 2016: TERENO: German network of terrestrial environmental observatories. *Journal of large-scale research facilities JLSRF*, **2**, A52–A52.

Chalapathy, R., and S. Chawla, 2019: Deep learning for anomaly detection: A survey. *arXiv preprint arXiv:1901.03407*.

Chen, M., Z. Wei, Z. Huang, B. Ding, and Y. Li, 2020: Simple and deep graph convolutional networks. *International conference on machine learning*, PMLR, 1725–1735.

Choi, H., C. Jung, T. Kang, H. J. Kim, and I.-Y. Kwak, 2022: Explainable time-series prediction using a residual network and gradient-based methods. *IEEE Access*, **10**, 108 469–108 482, https://doi.org/10.1109/access.2022.3213926.

Chwala, C., F. Keis, and H. Kunstmann, 2016: Real-time data acquisition of commercial microwave link networks for hydrometeorological applications. *Atmospheric Measurement Techniques*, **9 (3)**, 991–999.

Chwala, C., and H. Kunstmann, 2019: Commercial microwave link networks for rainfall observation: Assessment of the current status and future challenges. *WIREs Water*, **6 (2)**, e1337, https://doi.org/https://doi.org/10.1002/wat2.1337.

Cioffi, R., M. Travaglioni, G. Piscitelli, A. Petrillo, and F. De Felice, 2020: Artificial intelligence and machine learning applications in smart production: Progress, trends, and directions. *Sustainability*, **12 (2)**, 492.

Coley, C. W., W. Jin, L. Rogers, T. F. Jamison, T. S. Jaakkola, W. H. Green, R. Barzilay, and K. F. Jensen, 2019: A graph-convolutional neural network model for the prediction of chemical reactivity. *Chemical science*, **10 (2)**, 370–377.

Deng, A., and B. Hooi, 2021: Graph neural network-based anomaly detection in multivariate time series. *Proceedings of the AAAI conference on artificial intelligence*, Vol. 35, 4027–4035.

Egmont-Petersen, M., D. de Ridder, and H. Handels, 2002: Image processing with neural networks—a review. *Pattern recognition*, **35 (10)**, 2279–2301.

Erhan, L., M. Ndubuaku, M. Di Mauro, W. Song, M. Chen, G. Fortino, O. Bagdasar, and A. Liotta, 2021: Smart anomaly detection in sensor systems: A multi-perspective review. *Information Fusion*, **67**, 64–79.

Fan, W., Y. Ma, Q. Li, Y. He, E. Zhao, J. Tang, and D. Yin, 2019: Graph neural networks for social recommendation. *The world wide web conference*, 417–426.

Gandin, L. S., 1988: Complex quality control of meteorological observations. *Monthly Weather Review*, **116 (5)**, 1137–1156.

Graf, M., A. El Hachem, M. Eisele, J. Seidel, C. Chwala, H. Kunstmann, and A. Bárdossy, 2021: Rainfall estimates from opportunistic sensors in Germany across spatio-temporal scales. *Journal of Hydrology: Regional Studies*, **37**, 100 883, https://doi.org/10.1016/j.ejrh.2021.100883.

GSMA, 2022: The Mobile Economy 2022.

Guan, S., B. Zhao, Z. Dong, M. Gao, and Z. He, 2022: Gtad: Graph and temporal neural network for multivariate time series anomaly detection. *Entropy*, **24 (6)**, https://doi.org/10.3390/e24060759.

Horsburgh, J. S., S. L. Reeder, A. S. Jones, and J. Meline, 2015: Open source software for visualization and quality control of continuous hydrologic and water quality sensor data. *Environmental Modelling & Software*, **70**, 32–44, https://doi.org/10.1016/j.envsoft.2015.04.002.

Jiang, S., E. Bevacqua, and J. Zscheischler, 2022: River flooding mechanisms and their changes in europe revealed by explainable machine learning. *Hydrology and Earth System Sciences*, **26 (24)**, 6339–6359, https://doi.org/10.5194/hess-26-6339-2022.

Jones, A., T. Jones, and J. Horsburgh, 2022: Toward automating post processing of aquatic sensor data. *Environmental Modelling and Software*, **151**, 105 364, https://doi.org/10.1016/j.envsoft.2022.105364.

Jones, A. S., J. S. Horsburgh, and D. P. Eiriksson, 2018: Assessing subjectivity in environmental sensor data post processing via a controlled experiment. *Ecological Informatics*, **46**, 86–96, https://doi.org/10.1016/j.ecoinf.2018.05.001.

Kipf, T. N., and M. Welling, 2016: Semi-supervised classification with graph convolutional networks. *arXiv preprint arXiv:1609.02907*.

Kosasih, E. E., and A. Brintrup, 2022: A machine learning approach for predicting hidden links in supply chain with graph neural networks. *International Journal of Production Research*, **60 (17)**, 5380–5393, https://doi.org/10.1080/00207543.2021.1956697, https://doi.org/10.1080/00207543.2021.1956697.

Lin, X., H. Wang, J. Guo, and G. Mei, 2022: A deep learning approach using graph neural networks for anomaly detection in air quality data considering spatiotemporal correlations. *IEEE Access*, **10**, 94 074–94 088, https://doi.org/10.1109/ACCESS.2022.3204284.

Lorenz, C., and H. Kunstmann, 2012: The Hydrological Cycle in Three State-of-the-Art Reanalyses: Intercomparison and Performance Analysis. *Journal of Hydrometeorology*, **13 (5)**, 1397–1420, https://doi.org/10.1175/JHM-D-11-088.1.

Messer, H., A. Zinevich, and P. Alpert, 2006: Environmental Monitoring by Wireless Communication Networks. *Science*, **312 (5774)**, 713–713, https://doi.org/10.1126/science.1120034.

Mittelbach, H., I. Lehner, and S. I. Seneviratne, 2012: Comparison of four soil moisture sensor types under field conditions in switzerland. *Journal of Hydrology*, **430**, 39–49.

Muharemi, F., D. Logofătu, and F. Leon, 2019: Machine learning approaches for anomaly detection of water quality on a real-world data set. *Journal of information and telecommunication*, **3 (3)**, 294–307.

Nayak, J., K. Vakula, P. Dinesh, B. Naik, and D. Pelusi, 2020: Intelligent food processing: Journey from artificial neural network to deep learning. *Computer Science Review*, **38**, 100 297.

Polz, J., C. Chwala, M. Graf, and H. Kunstmann, 2020: Rain event detection in commercial microwave link attenuation data using convolutional neural networks. *Atmospheric Measurement Techniques*, **13 (7)**, 3835–3853, https://doi.org/https://doi.org/10.5194/amt-13-3835-2020.

Polz, J., L. Glawion, M. Graf, N. Blettner, E. Lasota, L. Schmidt, H. Kunstmann, and C. Chwala, 2023: Expert flagging of commercial microwave link signal anomalies: Effect on rainfall estimation and ambiguity of flagging. *2023 IEEE International Conference on Acoustics, Speech, and Signal Processing Workshops (ICASSPW)*, 1–5, https://doi.org/10.1109/ICASSPW59220.2023.10193654.

Pope, P. E., S. Kolouri, M. Rostami, C. E. Martin, and H. Hoffmann, 2019: Explainability methods for graph convolutional neural networks. *2019 IEEE/CVF Conference on Computer Vision and Pattern Recognition (CVPR)*, 10 764–10 773.

Rathee, M., T. Funke, A. Anand, and M. Khosla, 2022: Bagel: A benchmark for assessing graph neural network explanations. 2206.13983.

Rebmann, C., S. Claudia, M.-J. Sara, G. Sebastian, Z. Matthias, S. Luis, and C. Matthias, 2017: Integrative measurements focusing on carbon, energy and water fluxes at the forest site 'hohes holz' and the grassland 'am grossen bruch'. *EGU General Assembly Conference Abstracts*, 9727.

Rebmann, C., and Coauthors, 2018: ICOS eddy covariance flux-station site setup: a review. *International Agrophysics*, **32 (4)**, 471–494.

Russo, S., and Coauthors, 2021: The value of human data annotation for machine learning based anomaly detection in environmental systems. *Water Research*, **206**, 117 695, https://doi.org/https://doi.org/10.1016/j.watres.2021.117695.

Samek, W., G. Montavon, S. Lapuschkin, C. J. Anders, and K.-R. Müller, 2021: Explaining deep neural networks and beyond: A review of methods and applications. *Proceedings of the IEEE*, **109 (3)**, 247–278, https://doi.org/10.1109/jproc.2021.3060483.

Schmidt, L., and Coauthors, 2023: System for automated quality control (saqc) to enable traceable and reproducible data streams in environmental science. *Environmental Modelling and Software*, **169**, 105 809, https://doi.org/https://doi.org/10.1016/j.envsoft.2023.105809.

Shrikumar, A., P. Greenside, and A. Kundaje, 2017: Learning important features through propagating activation differences. *International conference on machine learning*, PMLR, 3145–3153, https://doi.org/10.48550/ARXIV.1704.02685.

Smilkov, D., N. Thorat, B. Kim, F. Viégas, and M. Wattenberg, 2017: Smoothgrad: removing noise by adding noise. *arXiv preprint arXiv:1706.03825*, https://doi.org/10.48550/ARXIV.1706.03825.

Sturtevant, C., S. Metzger, S. Nehr, and T. Foken, 2021: Quality assurance and control. *Springer Handbook of Atmospheric Measurements*, Springer, 47–90, https://doi.org/10.1007/978-3-030-52171-4_3.

SU, S. L., D. N. Singh, and M. S. Baghini, 2014: A critical review of soil moisture measurement. *Measurement*, **54**, 92–105.

Sundararajan, M., A. Taly, and Q. Yan, 2017: Axiomatic attribution for deep networks. *International conference on machine learning*, PMLR, 3319–3328, https://doi.org/10.48550/ARXIV.1703.01365.

Sutskever, I., O. Vinyals, and Q. V. Le, 2014: Sequence to sequence learning with neural networks. *Advances in neural information processing systems*, **27**.

UNFCCC, 2022: Sharm el-Sheikh Implementation Plan. Revised draft decision -/CMA.4 | UNFCCC. URL https://unfccc.int/documents/621908.

van Leth, T. C., A. Overeem, H. Leijnse, and R. Uijlenhoet, 2018: A measurement campaign to assess sources of error in microwave link rainfall estimation. *Atmospheric Measurement Techniques*, **11 (8)**, 4645–4669, https://doi.org/10.5194/amt-11-4645-2018.

Vandewinckele, L., M. Claessens, A. Dinkla, C. Brouwer, W. Crijns, D. Verellen, and W. van Elmpt, 2020: Overview of artificial intelligence-based applications in radiotherapy: Recommendations for implementation and quality assurance. *Radiotherapy and Oncology*, **153**, 55–66.

Wang, S., J. Cao, and P. S. Yu, 2022: Deep learning for spatio-temporal data mining: A survey. *IEEE Transactions on Knowledge and Data Engineering*, **34 (8)**, 3681–3700, https://doi.org/10.1109/TKDE.2020.3025580.

Wollschläger, U., and Coauthors, 2017: The bode hydrological observatory: a platform for integrated, interdisciplinary hydro-ecological research within the tereno harz/central german lowland observatory. *Environmental Earth Sciences*, **76 (1)**, 1–25, https://doi.org/10.1007/s12665-016-6327-5.

Yin, G., and Coauthors, 2023: Automatic recognition of schizophrenia from brain-network features using graph convolutional neural network. *Asian Journal of Psychiatry*, **87**, 103 687.

You, J., Z. Ying, and J. Leskovec, 2020: Design space for graph neural networks. *Advances in Neural Information Processing Systems*, **33**, 17 009–17 021.

Zhang, J., L. Pan, Q.-L. Han, C. Chen, S. Wen, and Y. Xiang, 2021: Deep learning based attack detection for cyber-physical system cybersecurity: A survey. *IEEE/CAA Journal of Automatica Sinica*, **9 (3)**, 377–391.

Zhang, M., S. Wu, X. Yu, Q. Liu, and L. Wang, 2022: Dynamic graph neural networks for sequential recommendation. *IEEE Transactions on Knowledge and Data Engineering*, **35 (5)**, 4741–4753.